ChemComm

Accepted Manuscript

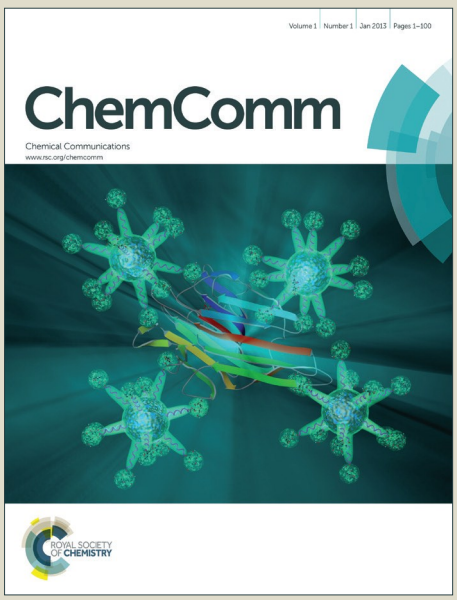

ROYAL SOCIETY OF CHEMISTRY

www.rsc.org/chemcomm

Cite this: DOI: 10.1039/x0xx00000x

Platinum nanoparticles encapsulated metal–organic frameworks for electrochemical detection of telomerase activity†

Received 00th January 2015,
Accepted 00th January 2015

DOI: 10.1039/x0xx00000x

www.rsc.org/

Pinghua Ling, Jianping Lei,* Li Jia and Huangxian Ju

A simple and rapid electrochemical sensor is constructed for detection of telomerase activity based on the electrocatalysis of platinum nanoparticles (Pt NPs) encapsulated metal-organic frameworks (MOFs), which are synthesized by one-pot encapsulation of Pt NPs into a prototypal MOFs, UiO-66-NH_2. Intergrating with the efficient electrocatalysis of Pt@MOFs towards $NaBH_4$ oxidation, this biosensor shows the widely dynamic correlation of telomerase activity from 5×10^2 to 10^7 HeLa cells mL^{-1} and the telomerase activity in single HeLa cell was calculated to be 2.0×10^{-11} IU, provided a powerful platform for detecting telomerase activity.

Telomerase consisting of $(TTAGGG)_n$ repeats,[1] has been regarded as both a cancer marker for early cancer diagnosis and a therapeutic target owing to its strong association with cell immortalization and tumorigenesis.[2] In most human somatic cells, the telomerase activity is highly depressed but telomerase has been observed over-expressed over 85% in human tumors.[3] The numerous methods have been developed to detect the telomerase activity, such as polymerase chain reaction,[4] electrochemiluminescence,[5] fluorescent method,[6] chemiluminescence[7] and electrochemical method.[8] Most of these developed probes provide the useful platform for telomerase assay. For example, a Cy5-tagged molecular beacon functionalized gold nanoparticle probe was designed for in situ fluorescent imaging and detection of cytoplasmic telomerase activity.[9] An electrochemical biosensor with ferrocene as the electroactive reporter was developed to detect telomerase activity via DNA structure-switching.[10] The signal readout of above methods always originates from the direct electrochemical signal or fluorescence "off"-"on" transduction. To trace the telomerase activity, an amplified signal, especially for catalytic signal, is highly desirable to design a facile and sensitive strategy.

Noble-metal nanoparticles (NPs), such as Au, Pd, and Pt, have been widely studied in heterogeneous catalysis owing to the unique structures. However, these free noble-metal NPs are easy to be aggregated. In order to overcome the drawback of NPs,[11] the most effort is to coat noble-metal NPs with either organic or inorganic shells such as silica,[12] zeolites,[13] and carbon.[14] Recently, metal-organic frameworks (MOFs), a new class of porous crystalline materials synthesized from metal ions/clusters and organic ligands,[15] have many applications in gas storage and separations,[16] sensing,[17] and drug delivery[18] owing to their high surface areas, well-defined porosities, and chemical tenability. In particular, MOFs as unique host matrices can offer a platform for incorporating metal nanoparticles to generate nanoparticle/MOFs composite,[19] which not only makes the metal NPs well-dispersion but also guarantees the MOF pores accessible for both reactant and product. There are two strategies to prepare nanoparticle/MOFs composites including encapsulating pre-synthesized nanoparticles in MOFs[20] or using MOFs as templates to generate nanoparticles within their cavities.[21] In the former, the spatial distribution of pre-synthesized nanoparticles embedded in the MOFs are hardly controlled. However, in the latter, it possesses inherent limitations such as aggregation of NPs on the external surface, the poor controlling of NPs size, and the potential damage of the MOFs structures during the post-reduction process of NPs. In addition, a one-step encapsulation of caffeine as model drug in MOF was demonstrated for high guest loading and controlled release.[22] In this work, we develop a one-pot strategy to prepare Pt NPs-encapsulated MOFs as electrocatalytic tracer for sensing telomerase activity.

Pt NPs-based nanomaterial with highly efficient catalysts toward the oxygen or 4-nitrophenol reduction has been utilized in the bioanalysis.[23,24] Especially, the electrocatalysis of Pt NPs towards $NaBH_4$ oxidation is multi-electron (maximum $8e^-$). Thus, the electrochemical signal produced in the process is much higher than those from the electrochemical reaction involving one-electron or two-electron oxidation. In view of the structural diversity and tenability of MOFs, we synthesized Pt NPs and MOFs composite (Pt@UiO-66-NH_2) via one-step, and sequentially immobilized with capture DNA (cDNA) as signal probe. Coupling with multi-electron electrocatalysis of Pt@UiO-66-NH_2 towards $NaBH_4$ oxidation, a signal-on electrochemical method was designed to detect telomerase activity from cancer cells (Scheme 1). Telomerase primer (TS), which could be extended in the presence of telomerase and dNTPs, was attached on glassy carbon electrode (GCE). After the telomerase primer extended, the Pt@UiO-66-NH_2-cDNA probe could hybrid with the extended part on the sensor surface, resulting in a significantly amplified electrocatalytic current towards $NaBH_4$ oxidation. This simple and rapid approach can detect the telomerase

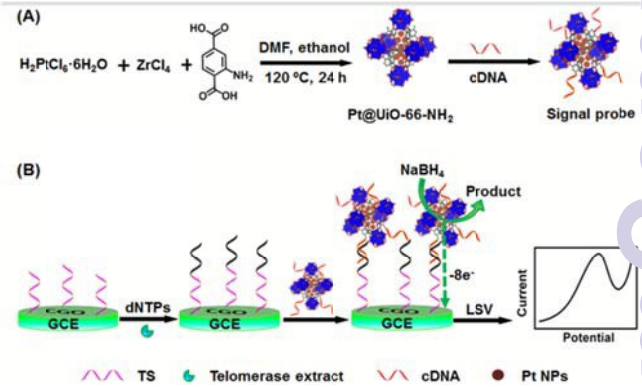

Scheme 1 Schematic representation of (A) Pt@UiO-66-NH_2 preparation and (B) Sensing principle for electrochemical detection of telomerase activity.

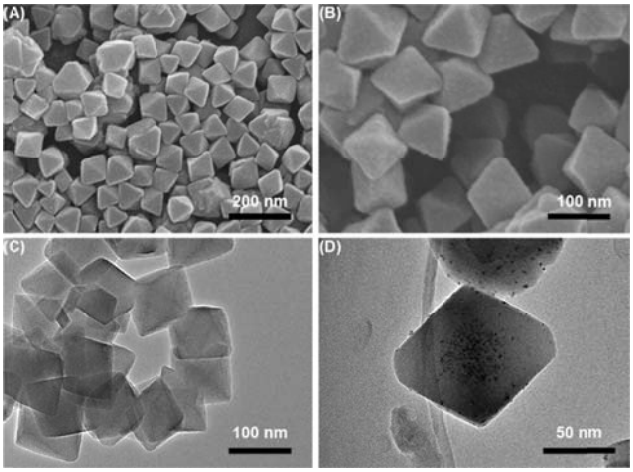

Fig. 1 SEM (A, B) and TEM (C, D) images of (A, C) UiO-66-NH_2 and (B, D) Pt@UiO-66-NH_2.

activity of HeLa extract in the wide range with a detection limit of 100 HeLa cells mL^{-1}, and the telomerase activity in single HeLa cell was also calculated. The Pt@MOF offers an excellent signal transduction platform for detection of telomerase activity, and could integrate with other recognition elements to broad the applications in bioassay.

UiO-66-NH_2 and Pt@UiO-66-NH_2 were synthesized by using 2-aminoterephthalic acid (NH_2-H_2BDC) as linker and Zr as node via solvothermal reaction. The morphology and structure of UiO-66-NH_2 and Pt@UiO-66-NH_2 nanocomposites are firstly investigated by different characterization techniques. The scanning electron microscopy (SEM) images of UiO-66-NH_2 and Pt@UiO-66-NH_2 showed that both crystal structures are octahedral geometry (Fig. 1A and 1B), which indicates the Pt NPs did not affect the octahemioctahedral crystal structure. No particles were observed on the surface, suggesting that the formed Pt NPs are well-dispersed inside the cavities of the MOFs. The transmission electron microscopy (TEM) images of UiO-66-NH_2 and Pt@UiO-66-NH_2 (Fig. 1C and 1D) exhibited intact crystal morphology with 100 nm. It is accordance with the result of dynamic light scattering (Fig. S1). Notably, Pt NPs were homogeneously distributed inside the UiO-66-NH_2 frameworks with the diameter of ~1.0 nm. During the synthesis of Pt@UiO-66-NH_2, DMF is utilized as both the solvent in NH_2-H_2BDC solution to directly determine the construction of UiO-66-NH_2, and the reducing agent for the effective formation of Pt NPs.[25]

The N_2 adsorption−desorption isotherm profiles and pore size distribution of UiO-66-NH_2 and Pt@UiO-66-NH_2 were shown in the Fig. 2A and 2B. Both adsorption−desorption isotherms show a type I shape, a typical characteristic of microporous materials. It is consistent with the result of pore size distribution (≤ 2.0 nm). The Brunauer–Emmett–Teller (BET) surface area and micropore volume of UiO-66-NH_2 were calculated to be 1128 $m^2\ g^{-1}$ and 0.44 $cm^3\ g^{-1}$, respectively. The BET surface area and pore volume of Pt@UiO-66-NH_2 had a little decrease (936 $m^2\ g^{-1}$ and 0.36 $cm^3\ g^{-1}$) compared with intrinsic UiO-66-NH_2, respectively, mainly due to the occupation of the cavities of UiO-66-NH_2 framework by Pt NPs. X-ray photoelectron spectroscopy (XPS) was used to investigate the surface composition of Pt@UiO-66-NH_2 composites (Fig. S2). Based on the XPS results, the Pt weight concentration was estimated to be 6.7% in the Pt@UiO-66-NH_2 composite.

The crystal structure and porosity of UiO-66-NH_2 and Pt@UiO-66-NH_2 composite were further characterized by X-ray diffraction (XRD). The XRD curves show the peaks at 14.48, 17.08, 19.16, 22.38, 25.18, and 30.88 degrees, which can be indexed to (222), (400), (420), (511), (600), and (640) of the octahedral geometry (JCPDF card number: 36−1452), indicating the octahemioctahedral crystal structure of MOF materials.[19b] Compared to the XRD spectrum of intrinsic UiO-66-NH_2 (Fig. 2C, curve a), no significant loss of crystallinity can be detected in the XRD pattern (Fig. 2C, curve b) after loading with Pt NPs, which is consistent with the result of thermogravimetric analysis in Fig. S3. Furthermore, the absence of XRD peaks from Pt nanocrystal could be presumably attributed to the low NPs concentration as well as the small size of encapsulated Pt particles in UiO-66-NH_2 framework.

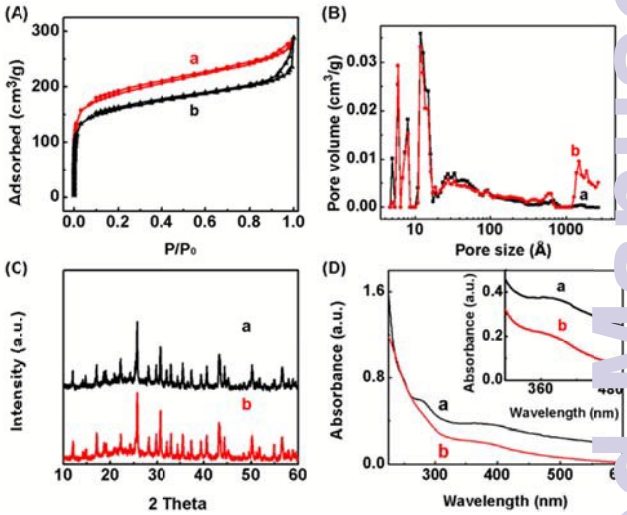

Fig. 2 (A) Nitrogen adsorption–desorption isotherm at 77 K, (B) DFT pore size distribution with N_2 at 77 K, and (C) Powder XRD patterns of UiO-66-NH_2 (a) and Pt@UiO-66-NH_2 (b). (D) UV-vis absorption spectra of Pt@UiO-66-NH_2-cDNA (a) and Pt@UiO-66-NH_2 (b).

In the fingerprint region of IR spectra (Fig. S4), the peak at 3507 cm^{-1}, 3384 cm^{-1}, 1500 cm^{-1} and 1250 cm^{-1} assigned to vasym (-NH_2), vsym (-NH_2), δ (-NH_2), and ν (C-N),[26] identifying the UiO-66-NH_2 functionalized with the group of -NH_2. In order to investigate the fabricated process of Pt@UiO-66-NH_2-cDNA, UV-vis absorption spectrometry was used (Fig. 2D). It showed that there was a new absorption peak at 278 nm (Fig. 2D, curve a) comparing with that of pure UiO-66-NH_2 (Fig. 2D, curve b), suggesting that DNA could be bound to Pt@UiO-66-NH_2 surface.

The electrocatalytic activity of different electrodes towards $NaBH_4$ oxidation was measured in 0.1 M pH 11.0 H_3BO_3-NaOH buffer with cyclic voltammograms (CVs). At the bare GCE and UiO-66-NH_2/GCE, there are not obvious signal in response to $NaBH_4$ in the examined potential range from −0.4 V to 0.6 V (Fig. 3A, curve a and curve b). However, it appeared two typical oxidation peaks at

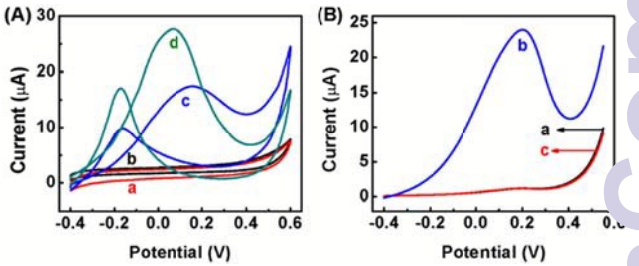

Fig. 3 (A) CVs of bare GCE (a), UiO-66-NH_2/GCE (b), Pt/GCE (c) and Pt@UiO-66-NH_2/GCE (d). (B) LSV responses of TS modified GCE incubated for 90 min in PBS + dNTPs (a), the extract + dNTPs (b) and the heated extract + dNTPs (c). The detection solution is in 0.1 M pH 11.0 H_3BO_3−NaOH buffer containing 5 mM $NaBH_4$. Scan rate: 50 mV s^{-1}.

around 0.08 V and -0.17 V corresponding to the oxidation of $NaBH_4$ at the Pt@UiO-66-NH_2/GCE and Pt/GCE electrode (Fig. 3A, curve c and d). Because $NaBH_4$ undergoes multi-electron (maximum $8e^-$) oxidation on Pt NPs,[27] the current signal could be much higher than those from the electrochemical reactions involving one-electron or two-electron oxidation.[28] Comparing with Pt/GCE, the Pt@UiO-66-NH_2/GCE showed large peak current, which identified the MOFs is an excellent support to load the Pt NPs for electrocatalysis.

The feasibility of the sensor was investigated by conducting linear sweep voltammetry (LSV) in response to $NaBH_4$ (Fig. 3B). When the TS modified GCE incubated with PBS (Fig. 3B, curve a) or heat-treated cell extract in the presence of dNTPs (Fig. 3B, curve c), the small peak current was observed due to the nonspecific adsorption between the UiO-66-NH_2 and the electrode surface. After treating with the telomerase extract, the TS on the electrode should be extended, and then hybridized with Pt@UiO-66-NH_2-cDNA. Thus, the Pt@UiO-66-NH_2 was introduced onto the GCE surface to catalyze towards $NaBH_4$ oxidation as detectable electrochemical signal (Fig. 3B, curve b).

Next, gel electrophoresis was employed to verify the feasibility of this method (Fig. S5). It illustrates different migration of TS (lane a) and cDNA (lane b) under the same condition. When TS was treated with the dNTPs and telomerase extract (lane c), a new band with low migration rate was appeared on the gel, which is consistent with the extension of about 1−2 telomere repeat segments synthesized by telomerase.[9] After incubating TS with heat-treated telomerase, the band is obtained at the same position of lane a (lane d), indicating the heat-treated telomerase losts its activity. When mixing TS and cDNA together, two individual bands show at the positions corresponding to TS and cDNA (line e), suggesting no hybridization between TS and cDNA in the absence of telomerase. In the presence of telomerase extract, the TS could be extended, and then hybridized with cDNA to form large molecular weight complex (lane f). These results showed that this biosensor is highly specific recognition in the detection of telomerase activity.

To ensure high hybridization efficiency and sensitivity, the TS density should be optimized (Fig. S6). When the primer concentration increased, the current reached to the maximum at 0.5 μM and then decreased, which was attributed to that the more TS on the electrode surface could hinder the extension of telomerase. The effect of incubation time and the hybridization time on the electrochemical response is also optimized (Fig. S7A and S7B). The current signal increased gradually up to 90 min and approached a platform (Fig. S7A). Therefore, 90 min was selected as the optimal incubation time for telomerase extension reaction. After the TS extension, the Pt@UiO-66-NH_2-cDNA would hybrid with the telomere repeats $(TTAGGG)_n$. The hybridization time between Pt@UiO-66-NH_2-cDNA and $(TTAGGG)_n$ is an important parameter that influences the signal. Upon the hybridization time more than 90 min, the current signal increased and reached a plateau (Fig. S7B). Thus, 90 min was selected as the hybridization time between Pt@UiO-66-NH_2-cDNA and $(TTAGGG)_n$ in the experiments.

The telomerase activity of cell extract was subsequently evaluated by performing telomerase extract from various concentrations of HeLa cells with LSV measurements under the optimal experimental conditions. The dynamic correlation between LSV peak current and telomerase activity demonstrates that electrochemical signal increased with the increasing of concentrations of HeLa cells ranging from 5×10^2 to 1×10^7 HeLa cells mL^{-1} (Fig. 4). The higher concentrations of HeLa cells, the more Pt@UiO-66-NH_2-cDNA was on the electrode surface, resulting in the enhanced catalytical current of Pt@UiO-66-NH_2 towards $NaBH_4$ oxidation. The inset of Fig. 4B shows that the signal from 500 cells could be easily distinguished from the background (Fig. 3B, curve a). The method demonstrates a good sensitivity with a detection limit of 100 HeLa cells mL^{-1} as calculated in terms of the rule of 3 times standard deviation over the blank response. This result could be comparable with the sensors reported by other groups.[7,8b]

Additionally, the present strategy possessed excellent repeatability with the obtained RSD of 3.8%, 4.0% and 4.6% in three repetitive assays of 500, 5000 and 10,000 HeLa cells. The reproducibility of the sensor was also studied, ten independently prepared electrodes were used with the RSD of 4.5%. When not in use, it was stored at 4 °C. After 2 weeks, the biosensor still retained 85% of the initial value. Therefore, the results indicated that the developed sensor had excellent repeatability and fabrication reproducibility, and acceptable stability. To detect the telomerase activity in each HeLa cell, the standard curve was obtained by using various concentrations of telomerase (10 μL) under the optimal experimental condition at TS modified GCE (Fig. S8). The telomerase activity was calculated to be 2.0×10^{-11} IU in each HeLa cell, which was slightly less than that of efficient Au NP probe-based fluorescence resonance energy transfer system (2.9×10^{-11} IU).[9]

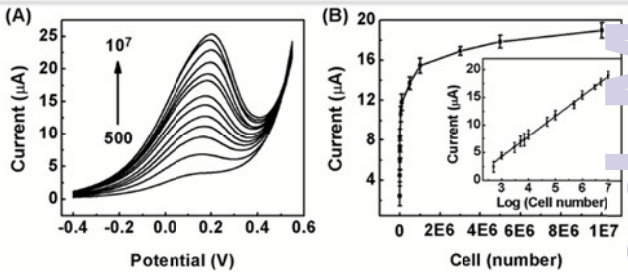

Fig. 4 LSV signals of a range of HeLa cell numbers (from bottom to top): 5×10^2, 10^3, 3×10^3, 5×10^3, 7×10^3, 10^4, 5×10^4, 10^5, 5×10^5, 10^6, 3×10^6, 5×10^6 and 10^7 cells mL^{-1}. (B) The plot of LSV peak currents vs. HeLa cell concentrations. Inset is the corresponding LSV peak currents vs. the logarithm of HeLa cell concentrations.

To demonstrate the reliability of this method for telomerase detection, other cancer cell lines such as U87, CEM, HEpG2 and MCF-7 cell lines were tested (Fig. 5). As expected, all of these cell lines showed positive telomerase activity, except for the heated HeLa cells sample which is due to the lack of telomerase activity after heating, so it showed a weak signal as background. According to the peak current, the telomerase activity of HeLa was higher than that of MCF-7, U87, CEM and HEpG2. These results were consistent with the previous reports that the telomerase could be detected in nearly 85% of human cancer cells, indicating the reliability of our method.

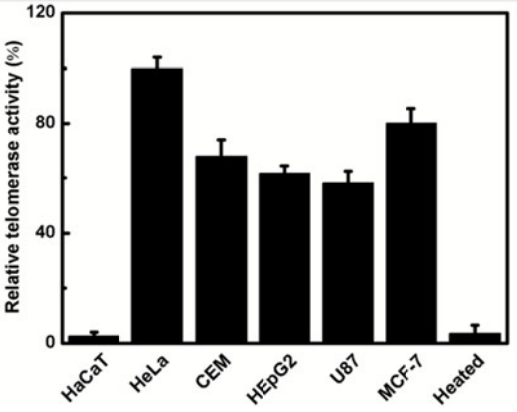

Fig. 5 Solid-state electrochemical assay to analyze telomerase activities in different cell lines. The telomerase activity of each cell line and negative heated control was normalized to HeLa cell. All the cell extracts were equivalent to 2000 cells.

In summary, this work successfully developed a one-pot strategy to prepare Pt NPs-encapsulated MOFs as electrocatalytic tracer for the rapid and sensitive electrochemical detection of telomerase activity. Owing to the well-defined porosities and chemical tenability of MOFs, the Pt NPs were homogeneously distributed inside the MOF frameworks with the diameter of ca. 1.0 nm. The resulting Pt@UiO-66-NH_2 composite demonstrated high electrocatalysis for $NaBH_4$ oxidation via multi-electron (maximum $8e^-$) transfer in alkaline solution. On the basis of the high catalytic performance of Pt@UiO-66-NH_2, the designed method can measure the telomerase activity with high sensitivity down to 100 cell mL^{-1} and wide dynamic range. More significantly, this approach achieved the detection of the telomerase activity in single cell. Furthermore, the proposed method is more convenient without the need for any additional separation steps. The advantages of the biosensor were also identified by analyzing various other cell lines of telomerase activity. The Pt@MOFs not only offer an excellent platform for elucidating the biofunctionality of telomerase but also easily integrate other signal amplification for trace detecting a wide range of the analysts.

This research was supported by the National Natural Science Foundation of China (21375060, 21135002, 21121091) and Priority development areas of the National Research Foundation for the Doctoral Program of Higher Education of China (20130091130005).

Notes and references

State Key Laboratory of Analytical Chemistry for Life Science, School of Chemistry and Chemical Engineering, Nanjing University, Nanjing 210093, P.R. China. E-mail: jpl@nju.edu.cn, Fax/Tel: +86 25 83593593.

† Electronic Supplementary Information (ESI) available: Experimental details and additional figures. See DOI:10.1039/c000000x/.

1 (a) E. H. Blackburn, *Nature*, 1991, **350**, 569−573; (b) S. B. Cohen, M. E. Graham, G. O. Lovrecz, N. Bache, P. J. Robinson and R. R. Reddel, *Science*, 2007, **315**, 1850−1853; (c) F. Rodier and J. Campisi, *J. Cell Biol.*, 2011, **192**, 547–556.

2 J. W. Shay and W. E. Wright, *Cancer Cell*, 2002, **2**, 257–265.

3 (a) K. Masutomi, E. Y. Yu, S. Khurts, I. Ben-Porath, J. L. Currier, G. B. Metz, M. W. Brooks, S. Kaneko, S. Murakami, J. A. DeCaprio, R. A. Weinberg, S. A. Stewart and W. C. Hahn, *Cell*, 2003, **114**, 241–253; (b) E. Kavaler, J. Landman, Y. Chang, M. J. Droller and B. C. S. Liu, *Cancer*, 1998, **82**, 708–714.

4 Y. Xiao, K. Y. Dane, T. Uzawa, A. Csordas, J. R. Qian, H. T. Soh, P. S. Daugherty, E. T. Lagally, A. J. Heeger and K. W. Plaxco, *J. Am. Chem. Soc*., 2010, **132**, 15299–15307.

5 (a) L. Wu, J. S. Wang, L. Y. Feng, J. S. Ren, W. L. Wei and X. G. Qu, *Adv. Mater.*, 2012, **24**, 2447–2452; (b) H. R. Zhang, M. S. Wu, J. J. Xu and H. Y. Chen, *Anal. Chem.*, 2014, **86**, 3834–3840.

6 (a) H. B. Wang, S. Wu, X. Chu and R. Q. Yu, *Chem. Commun.*, 2012, **48**, 5916–5918; (b) C. F. Ding, X. L. Li, Y. Ge and S. S. Zhang, *Anal. Chem.*, 2010, **82**, 2850–2855.

7 Y. Li, X. Li, X. T. Ji and X. M. Li, *Biosens. Bioelectron.*, 2011, **26**, 4095–4098.

8 (a) Y. Li, Y. L. Wen, L. L. Wang, W. Liang, L. Xu, S. Z. Ren, Z. Y. Zou, X. L. Zuo, C. H. Fan, Q. Huang, G. Liu and N. Q. Jia, *Biosens. Bioelectron.*, 2015, **67**, 364–369; (b) W. Q. Yang, X. Zhu, Q. D. Liu, Z. Y. Lin, B. Qiu and G. N. Chen, *Chem. Commun.*, 2011, **47**, 3129–3131.

9 R. C. Qian, L. Ding, L. W. Yan, M. F. Lin and H. X. Ju, *Anal. Chem.*, 2014, **86**, 8642–8648.

10 Z. Yi, H. B. Wang, K. Chen, Q. Gao, H. Tang, R. Q. Yu and X. Chu, *Biosens. Bioelectron.*, 2014, **53**, 310–315.

11 C. B. Gao, Q. Zhang, Z. D. Lu and Y. D. Yin, *J. Am. Chem. Soc.*, 2011, **133**, 19706–19709.

12 J. Wei, H. Wang, Y. H. Deng, Z. K. Sun, L. Shi, B. Tu, M. Luqman and D. Y. Zhao, *J. Am. Chem. Soc.*, 2011, **133**, 20369–20377.

13 Y. S. Tao, H. Kanoh, L. Abrams and K. Kaneko, *Chem. Rev.*, 2006, **106**, 896–910.

14 (a) Y. Wan, H. F. Yang and D. Y. Zhao, *Acc. Chem. Res.*, 2006, **39**, 423–432; (b) T. Harada, S. Ikeda, Y. H. Ng, T. Sakata, H. Mori, T. Torimoto and M. Matsumura, *Adv. Funct. Mater.*, 2008, **18**, 2190–2196.

15 O. K. Farha and J. T. Hupp, *Acc. Chem. Res.*, 2010, **43**, 1166–1175.

16 (a) D. X. Xue, A. J. Cairns, Y. Belmabkhout, L. Wojtas, Y. L. Liu, M. R. Alkordi and M. Eddaoudi, *J. Am. Chem. Soc.*, 2013, **135**, 7660–7667; (b) S. Keskin, T. M. van Heest and D. S. Sholl, *ChemSusChem*, 2010, **3**, 879–891.

17 (a) L. E. Kreno, K. Leong, O. K. Farha, M. Allendorf, R. P. Van Duyne and J. T. Hupp, *Chem. Rev.*, 2012, **112**, 1105–1125; (b) C. B. He, K. D. Lu and W. B. Lin, *J. Am. Chem. Soc.*, 2014, **136**, 12253–12256.

18 (a) C. B. He, K. D. Lu, D. M. Liu and W. B. Lin, *J. Am. Chem. Soc.*, 2014, **136**, 5181–5184; (b) S. Rojas, P. S. Wheatley, E. Quartapelle-Procopio, B. Gil, B. Marszalek, R. E. Morris and E. Barea, *CrystEngComm*, 2013, **15**, 9364–9367.

19(a) M. T. Zhao, K. Deng, L. C. He, Y. Liu, G. D. Li, H. J. Zhao and Z. Y. Tang, *J. Am. Chem. Soc.*, 2014, **136**, 1738–1741; (b) W. N. Zhang, G. L. Li, C. L. Cui, Y. Y. Liu, S. Z. Li, W. J. Yan, C. Xing, Y. R. Chi, Y. H. Yang and F. W. Huo, *Adv. Mater.*, 2014, **26**, 4056–4060.

20 (a) P. Falcaro, A. J. Hill, K. M. Nairn, J. Jasieniak, J. I. Mardel, T. J. Bastow, S. C. Mayo, M. Gimona, D. Gomez, H. J. Whitfield, R. Riccò, A. Patelli, B. Marmiroli, H. Amenitsch, T. Colson, L. Villanova and D. Buso, *Nat. Commun.*, 2011, **2**, 237; (b) M. R. Lohe, K. Gedrich, T. Freudenberg, E. Kockrick, T. Dellmann and S. Kaskel, *Chem. Commun.*, 2011, 3075–3077.

21 (a) D. Esken, S. Turner, O. I. Lebedev, G. V. Tendeloo and R. A. Fischer, *Chem. Mater.*, 2010, **22**, 6393–6401; (b) H. L. Jiang and Q. Xu, *Chem. Commun.*, 2011, **47**, 3351–3370; (c) X. J. Gu, Z. H. Lu, H. L. Jiang, T. Akita and Q. Xu, *J. Am. Chem. Soc.*, 2011, **133**, 11822–11825.

22 (a) N. Liédana, A. Galve, C. Rubio, C. Téllez and J. Coronas, *ACS Appl. Mater. Interfaces*, 2012, **4**, 5016−5021; (b) N. Liédana, P. Lozano, A. Galve, C. Télleza and J. Coronas, *J. Mater. Chem. B*, 2014, **2**, 1144–1151.

23 C. Z. Zhu, G. H. Yang, H. Li, D. Du and Y. H. Lin, *Anal. Chem.*, 2015, **87**, 230−249.

24 (a) S. F. Fu, G. H. Yang, Y. Z. Zhou, H. B. Pan, C. M. Wai, D. Du and Y. H. Lin, *RSC Adv.*, 2015, **5**, 32685–32689; (b) J. Tang, J. Zhou, Q. F. Li, T. P. Tang, G. N. Chen and H. H. Yang, *Chem. Commun*., 2013, **49**, 1530–1532.

25 (a) H. Yamamoto, H. Yano, H. Kouchi, Y. Obora, R. Arakawa and H. Kawasaki, *Nanoscale*, 2012, **4**, 4148–4154; (b) L. Rodríguez-Lorenzo, R. de la Rica, R. A. Álvarez-Puebla, L. M. Liz-Marzán and M. M. Stevens, *Nat. Mater.*, 2012, **11**, 604–607.

26 M. Kandiah, M. H. Nilsen, S. Usseglio, S. Jakobsen, U. Olsbye, M. Tilset, C. Larabi, E. A. Quadrelli, F. Bonino and K. P. Lillerud, *Chem. Mater.*, 2010, **22**, 6632–6640.

27 C. P. de Leon, F. C. Walsh, D. Pletcher, D. J. Browning and J. B. Lakeman, *J. Power Sources*, 2006, **155**, 172–181.

28 J. Das, H. Kim, K. Jo, K. H. Park, S. Y. Jon, K. Lee and H. Yang, *Chem. Commun.*, 2009, 6394–6396.